

# Finite-size and disorder effects on 1D unipartite and bipartite surface lattice resonances

ARAN WARREN,<sup>1,2,\*</sup>  MAAN M. ALKAISI,<sup>1,2</sup> AND CIARAN P. MOORE<sup>1</sup> 

<sup>1</sup>*Department of Electrical and Computer Engineering, University of Canterbury, Christchurch, New Zealand*

<sup>2</sup>*The MacDiarmid Institute for Advanced Materials and Nanotechnology, Wellington, New Zealand*

\**aran.warren@pg.canterbury.ac.nz*

**Abstract:** Optical resonances in bipartite metal nanostructure lattices are more resilient to finite size-effects than equivalent unipartite lattices, but the complexities of their behaviour in non-ideal settings remain relatively unexplored. Here we investigate the quality factor and extinction efficiency of 1D Ag and Au unipartite and bipartite lattices. By modelling finite size lattices over a range of periods we show that the quality factor of Ag bipartite lattices is significantly better than unipartite lattices. This improvement is less pronounced for Au bipartite lattices. We also show that bipartite lattices are dramatically affected by structure size variations at scales that are typically seen in electron beam lithography fabrication in contrast to unipartite lattices, which are not as sensitive.

© 2022 Optica Publishing Group under the terms of the [Optica Open Access Publishing Agreement](#)

## 1. Introduction

Optical resonators, operating in the visible spectrum, are critical components in many technologies, including lasers [1–4]. Recent advances in micro- and nano-fabrication techniques allow optical resonators to be built on the sub-wavelength scale, which has enabled the fabrication of metasurfaces [5], optical sensors [6] and nanolasers [1]. An example of an optical resonator is a metal spheroid, which is commonly used to model more irregular shapes which are fabricated with lithography and lift-off [7].

A metal sphere with a diameter on the order of 100 nm can exhibit an optical resonance due to the collective oscillation of free electrons in the metal, known as localised surface plasmon resonance (LSPR) [8]. A lattice of such structures with a period close to the wavelength of light can exhibit surface lattice resonance (SLR) due to the coherent scattering between many structures [9]. This has been found in both metal and dielectric lattices [10–15]. SLR has a much higher quality factor (Q) than LSPR that enables many innovative applications, including advanced sensors [16–19], laser cavities [2–4] and metasurfaces [20,21]. Tuning the period of the lattice, the surrounding refractive index, or the structure sizes leads to high quality resonances, localised and enhanced electric fields, and high scattering efficiencies [12,22,23]. Such tuneability also allows for precise control over the resonant wavelength, which has been used to realise wavelength tunable lasers [4] and reconfigurable metalenses [20].

Fabricated lattices inevitably suffer from some degree of disorder, either due to variations in the structure size or position or due to the introduction of defects, such as missing elements. It has been shown that SLR is very robust to the removal of elements in the lattice [24] and many studies have investigated the effect of positional disorder [24–31]. Disorder of the structure shape within the lattice has seen less attention, primarily due to the difficulty in modeling large lattices where all the elements are different and the challenge of controlling shape disorder experimentally [29,32–34]. Nevertheless, understanding the effect that size disorder has on SLR is increasingly important as fabrication moves from slow but precise methods such as electron beam lithography (EBL) to larger scale methods, such as nano-imprint lithography [35,36], which are expected

to exhibit larger error. Furthermore, plasmonic lattices are commonly fabricated using metal lift-off that, regardless of patterning method, introduces more structure disorder than the etching methods that are commonly used for dielectric lattices [37].

Finite-size effects are also an important consideration when designing plasmonic lattices. For some applications, large area ( $\text{cm}^2$ ) lattices are used that can be modelled as infinite lattices but for other applications, such as miniaturised lasers [38], finite lattices are required. A number of groups have shown a clear reduction of the quality factor in comparison to infinite lattices as the number of structures is reduced [15,33,38–41].

In addition to lattices comprising a single structure size, which we refer to as unipartite lattices, there is interest in lattices with multiple structure sizes that can exhibit enhanced quality factors and multiple resonances [39,42,43]. Recently bipartite lattices, consisting of two interlaced arrays with square symmetry but different structure sizes, were shown to exhibit quality factors much greater than that of the commonly used unipartite lattices [39]. It was also shown that these resonances require fewer interacting structures to achieve a given quality factor compared to unipartite lattices. This suggests that bipartite lattices may also be more robust to fabrication errors such as lattice dislocations. However, due to the strong dependence of the quality factor on the size difference between the constituent structures it is unclear how detrimental structure shape disorder would be in comparison to unipartite lattices. Motivated by the realisation of finite lattices with high quality factors, we explore the effect of varying period and number of structures on 1D finite unipartite and bipartite lattice resonances. We then investigate the effect that structure shape disorder has and make a comparison between unipartite and bipartite lattices.

Our results show how finite-size effects impact extinction efficiency and quality factors of Ag and Au lattice at visible wavelengths. We demonstrate that while bipartite lattices show much higher quality factors than unipartite lattices in general, consideration of the peak extinction efficiency and material properties are important when considering the applicability of these lattices. We also find that, despite the high Q resonances achieved with ideal bipartite lattices, they are strongly influenced by size disorder in comparison to unipartite lattices. These results emphasise the importance of considering multiple sources of fabrication error when assessing the suitability of more complex lattice resonances for practical applications.

## 2. Resonance mechanism

The systems studied in this work consist of 1D periodic lattices of metal nano-spheres, as shown in Fig. 1. The size of the structures and the period is chosen such that lattice resonances are observable in the visible spectrum. We note here that 1D lattices support similar resonances as 2D lattices yet can be modelled with fewer computational resources, and in general the resonances from a 1D lattice have a higher quality factor than their 2D counterparts [22]. Hence, these results are expected to apply qualitatively to 2D cases but will not show quantitative agreement. In Fig. 1(a) lattice A comprises silver spheres with a diameter ( $D_1$ ) of 100 nm and a period ( $p$ ) of 480 nm. The structures in lattice B have the same material properties and period as lattice A but a diameter ( $D_2$ ) of 90 nm. The bipartite lattice depicted in Fig. 1(b) is a combination of lattices A and B with a half period offset between the two lattices. In all cases the unit cell of these lattices has a length of  $p$  in the  $x$  direction. We take values for the complex refractive index of Ag from Johnson and Christy [44].

Due to the periodicity of the lattices their behavior is similar to that of diffraction gratings. By adjusting the period or refractive index it is possible to achieve diffraction orders that travel in the plane of the lattice. The wavelength where this occurs is known as the Rayleigh anomaly ( $\lambda_{RA}$ ). For normally incident light the lowest order RA has a wavelength given by  $\lambda_{RA} = p \cdot n$ , where  $p$  is the period of the lattice and  $n$  is the refractive index.

The lattice elements we consider in this work are metal spheres which can host LSPR. At the resonance wavelength,  $\lambda_{LSPR}$ , a large fraction of the incident power can be transferred into

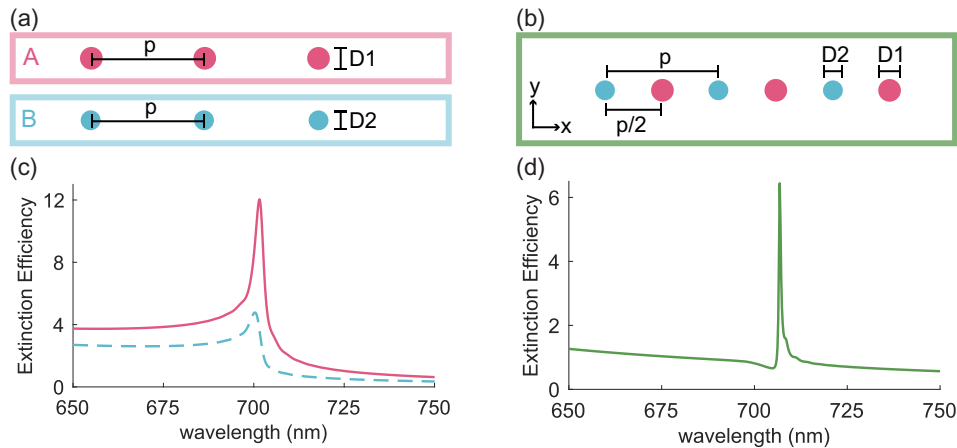


**Fig. 1.** (a) Diagram of the unipartite lattices A and B with 200 unit cells each. The structures are Ag spheres and  $D1$  is 100 nm,  $D2$  is 90 nm and  $p$  is 480 nm (b) Bipartite lattice constructed from lattices A and B offset by  $p/2$ . (c) Extinction efficiency spectrum for lattice A (solid) and lattice B (dashed). (d) Extinction efficiency spectrum for the bipartite lattice.

LSPR, resulting in a strong enhancement of electric field around the structure as well as increased scattering and absorption of the incident light. The spheres can be modeled as electric dipoles with complex polarisabilities, hence there is a phase difference between the incident and the scattered light from the sphere, which explains the spectral position of SLR peaks,  $\lambda_{SLR}$ .

Diffraction orders with wavelengths larger than  $\lambda_{RA}$  do not propagate away from the lattice but can be described as surface waves which propagate in the plane of the lattice and are evanescent in the direction normal to the lattice. The dampening of these surface waves increases as the wavelength is increased. SLR occurs when the scattered light from many structures arrives in phase with the incident light on neighbouring structures. Due to the phase delay between the incident light and resonantly scattered light an evanescent mode is required to achieve this resonance, i.e.  $\lambda_{SLR} > \lambda_{RA}$ .

The detuning between the RA and LSPR is defined as the wavelength difference between  $\lambda_{LSPR}$  and the  $\lambda_{RA}$ . In the case of small detuning, where  $\lambda_{RA}$  is chosen to be close to  $\lambda_{LSPR}$ , the effect of resonant scattering due to LSPR is large and a highly damped evanescent wave is required to satisfy the phase matching requirement of SLR. Due to the short propagation distance of evanescent waves the minimally detuned SLR require fewer interacting structures to achieve their maximum quality factor [33,45,46]. When detuning is increased, by moving  $\lambda_{RA}$  to much higher wavelengths than  $\lambda_{LSPR}$ ,  $\lambda_{SLR}$  approaches  $\lambda_{RA}$  due to coupling through weakly damped evanescent waves which are not perturbed as strongly by the LSPRs. These waves can travel long distances in the lattice, resulting in a much higher quality factor resonance than the less detuned lattices, at the expense of requiring a large number of interacting structures.

The bipartite lattices that we consider consist of two unipartite lattices interlaced such that there is a half period offset between them, as shown in Fig. 1(b). In this case there are two structures within the lattice unit cell, one with a diameter of  $D1$  and another with a diameter of  $D2$ . If  $D1 = D2$  then the scattering strength of each structure is the same and no resonance can occur because light radiated from structure 1 will arrive out-of-phase with the resonance in structure 2. However, when  $D1 > D2$ , structure 1 is a stronger scatterer if all other parameters are the same. Hence, it is able to polarise structure 2 such that it is out-of-phase [39]. In this case light radiated from structure 1 arrives in phase with structure 2, resulting in coherent coupling. With both elements out-of-phase with respect to each other destructive interference reduces

light scattering away from the lattice. This dramatically increases the quality factor due to the reduction in radiative loss, hence these resonances are commonly referred to as ‘sub-radiant’ [39,47].

### 3. Model

The extinction spectra for ideal unipartite lattices with 200 unit cells, which has 200 structures in total, are shown in Fig. 1(c). We modeled the lattices using SMUTHI [48], which implements the T-matrix method and has previously been used for finite disordered lattices [49,50]. The extinction spectrum for the bipartite lattice, also with 200 unit cells and 400 structures in total, is shown in Fig. 1(d). The extinction peak is clearly shifted to higher wavelengths (706.8 nm) than the RA (700.8 nm) and unipartite SLRs (701.6 nm and 700.4 nm), as expected. Furthermore, the quality factor is dramatically improved from 88 and 186 for the unipartite lattices with diameters of 90 nm and 100 nm, respectively, to 1090 for the bipartite lattice.

All results in this work were achieved by modeling the incident light as a normally incident plane wave polarised in the  $y$  direction and the wavelength resolution of all simulations was 0.2nm. The lattices were modeled in a uniform refractive index environment of  $n = 1.46$ . This was chosen as it is approximately the refractive index of fused quartz, which is a common substrate for optical elements.

The quality factor is defined as  $Q = f_0/\Delta f$ , where  $f_0$  is the centre frequency of the resonance and  $\Delta f$  is the peak width at half maximum. Because the spectra in Fig. 1 consists of two overlapping resonances, one a broad peak due to LSPR and the other a sharp peak from SLR, we first remove the background LSPR extinction before measuring the quality factor. The background removal was particularly required for peaks where the half maximum was less than the background level. Further details and an example of the background fitting can be seen in Section 1 and Figure S1 of Supplement 1. We have also utilised a figure of merit (FOM) equal to  $E_{max} \cdot Q$ , where  $E_{max}$  is the peak extinction efficiency at the SLR wavelength with the background extinction level subtracted. We report FOM values as some applications, such as biosensors or colour filters, require high peak extinction efficiencies and quality factors. The extinction efficiency is calculated by dividing the extinction cross-section ( $C_{ext}$ ), returned by the T-matrix model, by the geometric area of the lattice ( $A_{lattice}$ ) where the geometric area is determined by  $A_{lattice} = N \cdot \pi(D/2)^2$  for a unipartite lattice or  $A_{lattice} = N \cdot \pi[(D_1/2)^2 + (D_2/2)^2]$  for a bipartite lattice.

In this work we compare the quality factor of finite lattices to that of infinite lattices. There are methods for calculating the quality factor of infinite lattices based on the coupled dipole method [51]. However, to provide a quantitative comparison between an infinite and finite lattice with the T-matrix method we take the infinite quality factor to be the value of  $Q$  which does not change significantly with an increasing number of structures. Further details can be found in Figure S2 of Supplement 1.

### 4. Finite-size effects for unipartite lattices

To investigate finite size effects on the SLR quality factor we model 1D lattices with  $N = 40$  to  $N = 200$ , where  $N$  is the number of unit cells in the lattice. For a 500 nm period lattice this corresponds to a total length ranging from 20  $\mu\text{m}$  to 100  $\mu\text{m}$ . We also model periods between 400 nm and 500 nm in steps of 10 nm. We extend the range to  $p = 600$  nm for structure diameters of 122.5 nm and 126.5 nm. Increasing the period increases the detuning between  $\lambda_{LSPR}$  and  $\lambda_{RA}$ , resulting in higher quality resonances that are expected to require more unit cells to approach the infinite limit [33,46]. In these simulations  $\lambda_{RA}$  ranges from 584 nm to 730 nm for  $p = 400$  nm and  $p = 500$  nm, respectively, with  $\lambda_{RA} = 876$  nm for  $p = 600$  nm.

Figures 2(a)-(d) show  $Q$  against period for 1D lattices with a structure diameter of 90 nm, 100 nm, 122.5 nm and 126.5 nm, respectively. Each line in the plot represents a different choice of  $N$

as indicated by the black arrow in Fig. 2(a). In Figs. 2(e)-h we present  $E_{max}$  for the same lattices and in Figs. 2(i)-l we show the FOM

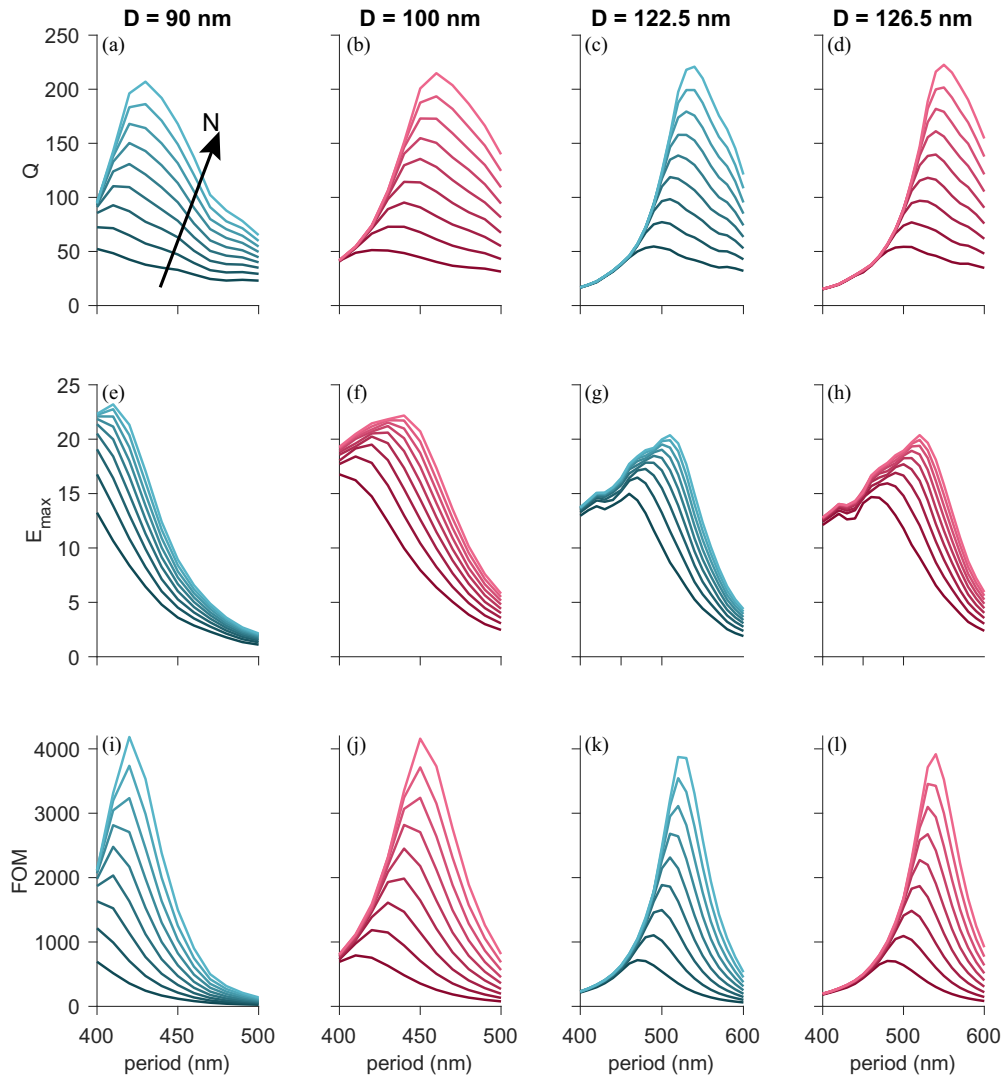


**Fig. 2.** Modeled finite size effect on unipartite Ag lattices with 90 nm spheres (a,e,i), 100 nm spheres (b,f,j), 122.5 nm spheres (c,g,k) and 126.5 nm spheres (d,h,l). Plots are for lattices of different sizes from  $N = 40$  (darkest shade) to  $N = 200$  (lightest shade) in steps of 20 and periods ranging from 400 nm to 500 nm (a,b,e,f,i,j) or 600 nm (c,d,g,h,k,l) in steps of 10 nm. In (a), (b), (c) and (d)  $Q$  is plotted against  $p$ . In (e),(f),(g) and (h) the peak extinction efficiency ( $E_{max}$ ) is plotted. (i),(j),(k) and (l) show the figure of merit (FOM) defined as  $Q \cdot E_{max}$ . All results are calculated using the T-matrix method with a uniform surrounding refractive index of 1.46.

We investigate both Ag and Au lattices: Ag is chosen for its attractive plasmonic properties and wide use in plasmonic applications [52], while Au is a popular material for plasmonic applications due to its stability and chemical resistance when compared to other popular materials such as Ag, Al and Cu [53]. As with the Ag lattices, Figs. 3(a) and 3(c) show  $Q$  and FOM for Au

lattices with a diameter of 90 nm. Figures 3(b) and 3(d) show the same but for lattices with 100 nm diameter spheres. We take the complex refractive index of Au from Johnson and Christy [44].

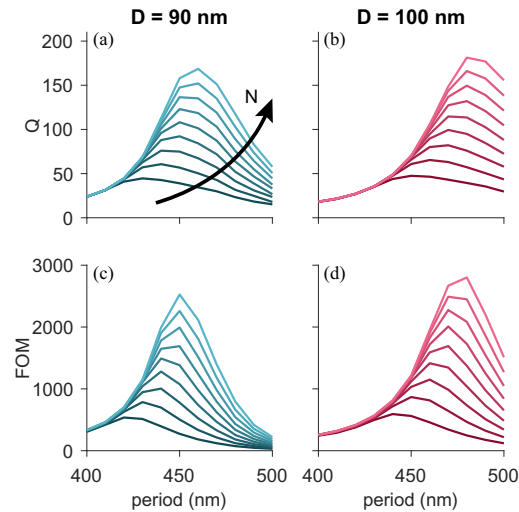


**Fig. 3.** Simulated finite size effect on unipartite Au lattices. The quality factor and figure of merit are plotted against period in (a - b) and (c - d), respectively. The results are shown for 90 nm spheres in (a) and (c) and 100 nm spheres in (b) and (d).

From the results in Fig. 2 and 3 it can be seen that, regardless of material and structure size, larger lattices are needed to achieve high quality factors as the detuning is increased in agreement with results shown by others [51]. Interestingly, quality factors quickly increase with increasing period for a given  $N$  and there is a point where the quality factor is limited by the finite size of the lattice, as evident from the deviation of the curves in Figs. 2(a)-(d), 3(a) and 3(b). After this point the curves peak and then increasing the period decreases the quality factor, although at a slower rate compared to the increase at lower periods.

In contrast to the quality factor results, the FOM rapidly decreases as period is increased, for all the unipartite lattices, once finite size effects become significant, as shown in Figs. 2(i)-(l), 3(c) and 3(d). This can be attributed to a decrease in the extinction efficiency as the period is increased to higher values, as shown in Figs. 2(e)-(h) for Ag lattices: the results for Au lattices, which show a similar trend, are shown in Figure S5 of Supplement 1. This results in a significant peak in the FOM curves for both Ag and Au lattices. At this point the increasing quality factor due to detuning balances the finite-size effects. Hence, if the goal is to achieve the highest FOM, for a given material and structure diameter there is an ideal period for a given  $N$ . These results highlight the importance of considering the peak extinction efficiency as well as the quality factor when designing finite lattices, as the peak extinction efficiency is even more sensitive to finite-size effects than the quality factor.

In addition to these general properties of finite lattices, there are some significant differences between the materials and structure sizes. Figures 2 and 3 show that unipartite lattices with both 90 nm and 100 nm diameter structures exhibit similar finite-size effects independent of material. However, the curve families appear to shift to higher periods as the diameter is changed from 90 nm to 100 nm, as seen by comparing Figs. 2(a) and 2(b) for Ag and Figs. 3(a) and 3(b) for Au. This indicates that the quality factor and deviation of the lattices from the infinite limit is highly dependent on the detuning between  $\lambda_{LSPR}$  and  $\lambda_{RA}$ . This also explains why the curves for Au lattices follow the same trend as the Ag lattices, albeit shifted to higher periods. This is because

$\lambda_{LSPR}$  for the Au spheres (593 nm for  $D = 100$  nm) is higher than for the Ag spheres (520 nm for  $D = 100$  nm), as shown in Figure S3 of [Supplement 1](#).

To investigate the effect of material properties without the influence of detuning we have also included Ag lattices with 122.5 nm and 126 nm structure diameters as shown in Figs. 2. In this case the 122.5 nm diameter Ag sphere has  $\lambda_{LSPR} = 580$  nm and the 126.5 nm diameter sphere has  $\lambda_{LSPR} = 592$  nm which is similar to the Au spheres with  $\lambda_{LSPR} = 580$  nm for the 90 nm diameter sphere and  $\lambda_{LSPR} = 593$  nm for the 100 nm diameter sphere, as shown in Figure S4 of [Supplement 1](#). When comparing the Au lattices to the Ag lattices with 122.5 nm and 126.5 nm diameter structures, where the detuning is the same, the Ag lattices require much larger periods to achieve similar quality factors to that of Au lattices. The origin of this phenomena can be attributed to the width of the LSPR peak. These results indicate that a larger quality factor for the LSPR peak will require less detuning of the RA to achieve a high quality factor in comparison to another structure with the same  $\lambda_{LSPR}$ .

Despite having higher LSPR extinction efficiencies, the FOMs for Au lattices, shown in Figs. 3(c) and 3(d), are reduced in comparison to Ag lattices with 90 nm and 100 nm diameter structure. This is expected, due to the reduced extinction efficiency associated with Au lattices compared to Ag, which can be attributed to the higher absorption that is expected in Au structures.

## 5. Finite-size Effects for Bipartite Lattices

Finite-size effects were also investigated for bipartite lattices. Firstly, we set  $D1 = 100$  nm and varied  $D2$  as shown in Fig. 4. Then, using a value for  $D2$  that gave the highest quality factor, we investigate changing period in the same way that was done for unipartite lattices, as shown in Fig. 5.

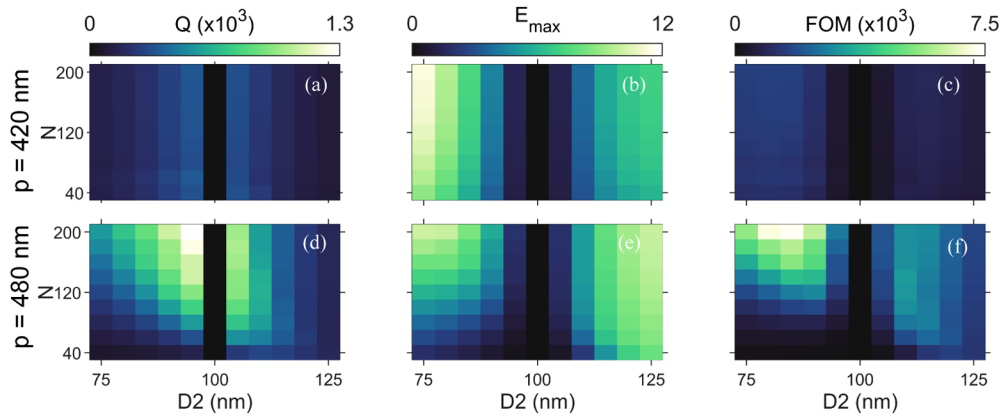


**Fig. 4.** Modeled finite size effects of bipartite Ag lattices with varying  $D2$ .  $D1$  is set to 100 nm and the period is set to 420 nm in (a), (b) and (c) and 480 nm in (d), (e) and (f). Plots are for lattices of different sizes with  $N$  from 40 to 200 and  $D2$  ranging from 75 nm to 125 nm in steps of 5 nm. In (a) and (d) quality factor is plotted against  $D2$ . In (b) and (e) the peak extinction efficiency ( $E_{max}$ ) is plotted. (c) and (f) show the figure of merit (FOM). All models assume a uniform surrounding refractive index of 1.46. When  $D1$  and  $D2$  are equal no resonance is observed, resulting in a null in all plots when  $D2 = 100$  nm. Linear interpolation between the data points is also used.

To determine an appropriate value for  $D2$ , finite lattices were modeled with  $D1$  of 100 nm and  $D2$  varying from 75 nm to 125 nm in steps of 5 nm, as shown in Fig. 4. In Fig. 4(a) and 4(d) we show the quality factor for bipartite lattices with a period of 420 nm and 480 nm, respectively. The corresponding peak extinction efficiency and FOM are presented in Figs. 4(b) and 4(e) and

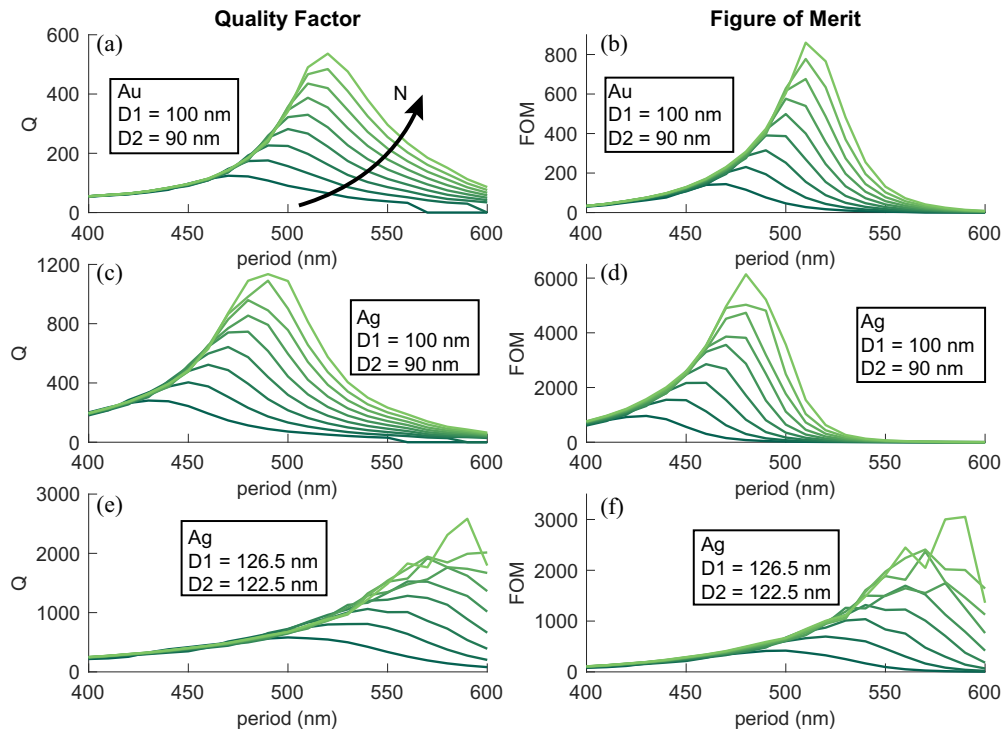


**Fig. 5.** Modeled finite size effect on bipartite Ag (a, c) and Au (b, d) sphere lattices with  $D1 = 90$  nm and  $D2 = 100$  nm. Plots are for lattices of different sizes from  $N = 40$  to  $N = 200$  in steps of 20 and periods ranging from 400 nm to 600 nm in steps of 10 nm. Darker curves correspond to lower  $N$ . In (a) and (b)  $Q$  is plotted against  $p$ . (c) and (d) show the FOM. All results are calculated with a uniform surrounding refractive index of 1.46 and a normally incident plan wave.

Figs. 4(c) and 4(f), respectively. These plots show two peaks in quality factor with resonance disappearing when  $D1$  and  $D2$  are equal at 100 nm, which is in agreement with previous work by others [39]. A sudden jump in quality factor is observed as the diameter resolution is only 5 nm; however, it is expected that there is a smooth, albeit rapid, transition to  $Q = 0$  when  $D1$  and  $D2$  are equal [39] rather than an infinite quality factor which would be indicative of a bound state in the continuum [43]. We base the rest of this work on  $D2 = 90$  nm as it produced the highest quality factor resonances at  $p = 420$  nm and  $p = 480$  nm.

For bipartite Ag lattices with  $D1 = 100$  nm and 420 nm period we can see that higher quality factors are achieved when  $D2$  is 90 nm than when  $D2$  is 110 nm, as shown in Fig. 4(a), despite the same diameter difference between  $D1$  and  $D2$ . This can be explained by considering that the detuning between  $\lambda_{LSPR}$  and  $\lambda_{RA}$  will decrease as  $D2$  is increased. This also suggests that increasing  $D2$ , for a given  $N$ , will bring the quality factor closer to that of an infinite lattice. This can be clearly seen in Fig. 4(d) where finite-size effects are significant when  $D2$  is less than 100 nm (evident from the changing  $Q$  with an increase in  $N$ ) and are reduced as  $D2$  is increased. Finite size effects are significantly reduced when  $D2$  is greater than 110 nm as shown by the minimal dependence of  $Q$  on  $N$  for these values of  $D2$ . Finite size effects are negligible at  $D2 = 125$  nm where  $Q$  does not change with  $N$  over the range that we have investigated here.

Figure 5 shows the effect of changing period on  $Q$  and FOM for finite Ag and Au bipartite lattices: data for  $E_{max}$ , is included in Figure S6 of Supplement 1. Here  $D1 = 100$  nm and  $D2 = 90$  nm for Figs. 5(a)-(c).  $D1 = 126.5$  nm and  $D2 = 122.5$  nm in Figs. 5(e) and f. In

all cases the period is varied from 400 nm to 600 nm. The results for Ag lattices are shown in Figs. 5(c)-(f) while the results for Au lattices are shown in Figs. 5(a) and (b).

These results have significant implications for finite bipartite lattices which have a high detuning between  $\lambda_{LSPR}$  and  $\lambda_{RA}$ . As seen in Fig. 5(c), for example, where for a given  $N$  there is an optimal period that produces the highest quality factor, which, similar to the unipartite lattices, is due to the balancing between an increase in  $Q$  due to detuning and a decrease in  $Q$  due to finite size effects. Finite lattices with periods larger than this optimal period can benefit from an increase in  $D2$  resulting in a reduction in detuning which will increase the quality factor and FOM, as seen for  $N = 40$  to  $N = 120$  in Figs. 4(d) and 4(f). Conversely, finite lattices that have periods less than or equal to their optimal period will be negatively impacted by an increase in  $D2$ .

In contrast to  $Q$ ,  $E_{max}$  decreases as  $|D1 - D2|$  decreases, as shown in Figs. 4(b) and 4(e). This results in the peak FOM shifting to higher values of  $|D1 - D2|$ , due to the balancing between a decreasing extinction efficiency and an increasing quality factor. When  $D1$  and  $D2$  are different, radiation and light coupling into the lattice are partially suppressed due to destructive interference. This destructive interference increases as the scattering efficiency of the structures equalise, ultimately resulting in no pathway for radiation when  $D1$  and  $D2$  are equal.

Similar to unipartite lattices, bipartite lattices show an increase in quality factor as the period is increased, as shown in Figs. 5(a),c and e. However, bipartite lattices typically exhibit higher quality factors than unipartite lattices for the same number of unit cells [39]. This is evident when comparing the  $Q$  for Ag bipartite lattices, shown in Fig. 5(c), to the unipartite lattices, shown in Fig. 2(a) for  $D = 90$  nm and in Fig. 2(b) for  $D = 100$  nm. Here the bipartite lattices can reach quality factors of over 1000, whereas none of the unipartite lattices achieve  $Q$  above 250. Furthermore, results for bipartite lattices with the same detuning as unipartite lattices can be seen by comparing Figs. 5(e) and (f) to Fig. 2(a) and (b). Here the bipartite lattice exhibits significantly higher quality factors than unipartite lattices despite the constituent elements having the same detuning for the RA. In Figs. 5(e) and (f) the quality factors reach above 2000, which is due to the limited wavelength resolution that results in low quality factor resolution at these small line widths. It is evident that the quality factor is significantly affected by the size difference between the elements rather than the detuning of LSPR and SLR, as expected from the results shown in Fig. 4.

## 6. Material effects in bipartite lattices

The quality factor is significantly lower for Au bipartite lattices, shown in Fig. 5(a), compared to Ag lattices. This results in close to an order of magnitude lower FOM than the Ag cases. The poor performance of the Au bipartite lattices, with FOMs worse than the Au unipartite lattices, can again be attributed to the higher dielectric loss in Au [44]. This may indicate that bipartite lattices are more sensitive to material loss than unipartite lattices, where the difference between Ag and Au is not as significant. This would be expected as the subradiant bipartite resonances arise from the interference of scattered light.

The finite-size effects for bipartite lattices of both materials exhibit similar properties to the unipartite lattices: for bipartite lattices finite-size effects occur at larger periods than for unipartite lattices; however, the FOM rapidly decreases at larger periods, in contrast to the unipartite lattices.

## 7. Structure diameter disorder effects

Next, we investigate disorder effects for Ag unipartite and bipartite lattices. Ag was chosen because the Au bipartite lattices behaved poorly over wavelength ranges considered in this work. For bipartite lattices it was hypothesised that the quality factor will be significantly diminished for lattices with structural disorder, due to the dependence of  $Q$  on the difference between  $D1$  and  $D2$ , as shown in Fig. 4, yet this has not been verified previously.

Each sphere diameter in the lattice was randomly generated from a Gaussian distribution with a mean of 90 nm or 100 nm and a standard deviation ( $\sigma$ ) of 5 nm. 5 nm was chosen as a realistic value that is close to what we have measured previously with lattices fabricated with electron beam lithography [54]. For each trial we used a set seed for the random number generator so that the period could be changed while preserving relative disorder. Ten trials were done with 10 different seeds, generating 10  $Q$  vs  $p$  curves. This was done for Ag unipartite lattices with  $D = 100$  nm for  $N = 60$ ,  $N = 100$  and  $N = 200$ . The quality factor results are shown in Fig. 6(a) and 6(b) and the corresponding FOM results are shown in Fig. 6(c) and 6(d). The dashed line shows the  $Q$  or FOM for an ideal lattice with no diameter deviation. The mean  $Q$  for each set of 10 disordered lattices is indicated by the solid line and the shaded region around the mean plots one standard deviation either side of the mean.

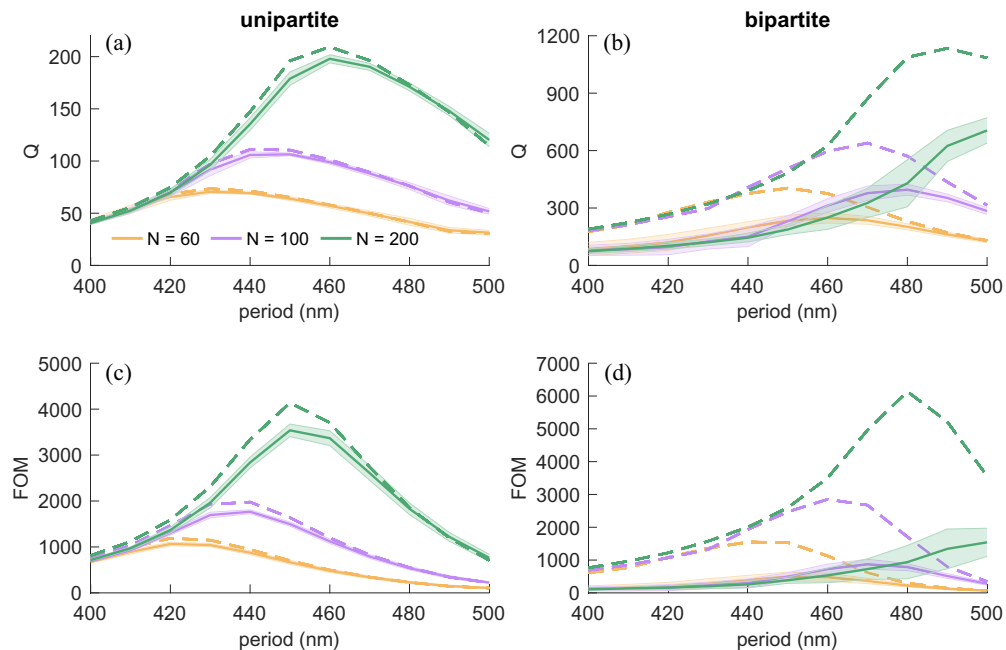


**Fig. 6.** The effect of disorder in unipartite and bipartite Ag lattices. (a) Quality factor vs period for three unipartite lattices with  $N$  of 60, 100 and 200 and  $D = 100$  nm. The dashed lines show the ideal quality factor taken from Fig. 2(a). The solid line shows the mean quality factor from 10 trials where each structure is randomly generated from a population with a standard deviation of 5 nm. The shaded area shows the standard deviation in quality factors. (b) Quality factor vs period for three bipartite lattices with  $D_1 = 100$  nm and  $D_2 = 90$  nm. The legend is the same as (a). (c) and (d) show the corresponding FOM for unipartite and bipartite lattices, respectively.

Figures 6(a) and 6(b) show clear differences between disordered unipartite and bipartite lattices. The quality factors of the unipartite lattices (Figure 6(a)) are only minimally reduced by the structure disorder over all periods. In contrast, bipartite lattices (Figure 6(b)) show a significant sensitivity to the structure deviation. For periods less than 440 nm the mean quality factor is at least halved for both  $N = 60$  and  $N = 200$ . Figure 7(a) and b show a comparison of unipartite and bipartite lattices over a limited period range where the effect of disorder on quality factor can be seen more clearly. In Fig. 7(a) at  $p = 450$  nm a minimal reduction in quality factor is observed for a unipartite lattice; however, the bipartite lattice shows a significant decrease

in quality factor at a period of 400 nm when the disorder is introduced, as shown in Fig. 7(b), despite both unipartite and bipartite lattices having similar quality factors under ideal conditions.

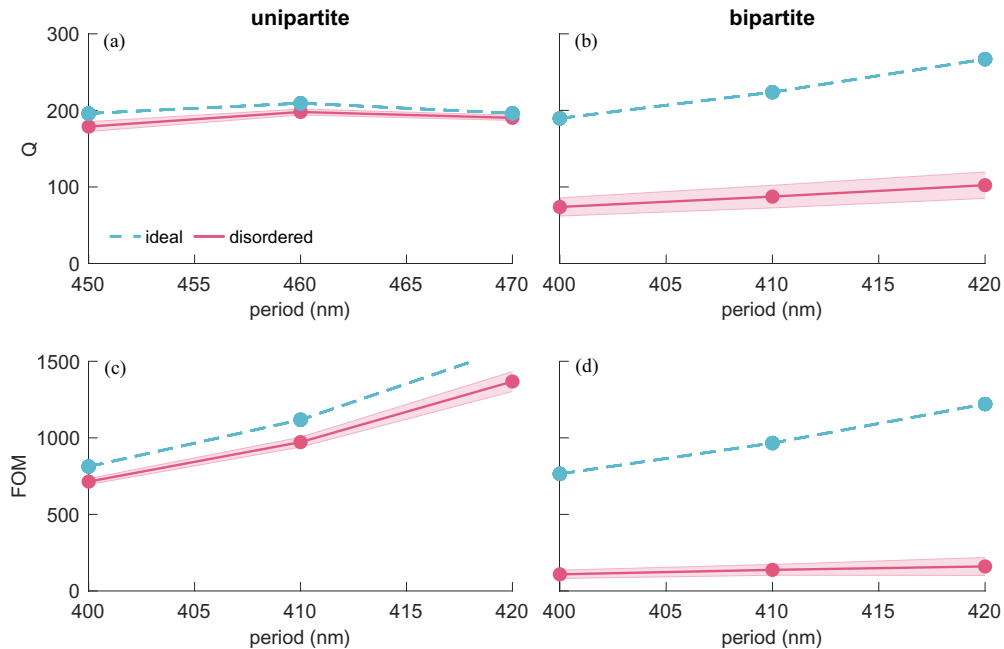


**Fig. 7.** Comparison of disorder in unipartite (a,c) and bipartite (b,d) lattices with similar quality factors (a,b) and similar figures of merit (c,d). The data is taken from Fig. 6 over a limited range of periods and restricted to  $N = 200$ .

The FOM results shown in Fig. 6(d) further emphasise the effect of disorder, where for the  $N = 200$  lattice the FOM is only  $\approx 15\%$  of the ideal value at  $p = 400$  nm and  $p = 480$  nm. This again contrasts with the unipartite case, shown in Fig. 6(c), where significantly less reduction in FOM is observed. Again, this is highlighted in Fig. 7 where the unipartite lattices shows a minimal reduction in FOM at  $p = 400$  nm, shown in Fig. 7(c), and the bipartite lattice is significantly affected, as shown in Fig. 7(d), despite having similar FOMs under ideal conditions

These results show that, while FOM for an ideal bipartite lattice is similar to that of the unipartite lattices, when structure disorder is accounted for bipartite lattices perform worse. For example, if we consider a 400 nm period Ag lattice with 200 unit cells, a FOM of 812.7 can be achieved for an ideal unipartite lattice, as shown in Fig. 7(c), and a FOM of 764.7 can be achieved for an ideal bipartite lattice, as shown in Fig. 7(d). With the introduction of a 5 nm standard deviation in diameter, the mean FOM is reduced to 108.6 for the bipartite lattice, which is now much less than the FOM of 714.3 for the unipartite lattice with the same deviation in structure size.

This has important implications for fabrication. We expect that both finite and approximately infinite bipartite lattices will suffer from a significant reduction in quality factor and extinction efficiency when these lattices are experimentally implemented. This could present a challenge in the application of these lattices. However, there may be some methods for mitigation: for example, annealing has been shown to reduce disorder and increase the quality factor of unipartite lattice resonance and could be used to achieve the same effect with bipartite lattices [55]. Using dielectric structures, such as silicon cylinders, may also be an option for some applications, as these are commonly fabricated with anisotropic etching methods which produce structures with very small diameter deviation [37].

## 8. Conclusion

In this work we have shown how the quality factor and extinction efficiency of 1D finite plasmonic lattices evolve with period and number of unit cells. We have found that, for a given number of unit cells, there exists a period for which the figure of merit is maximised. This is the case for both unipartite and bipartite lattices. Ideal bipartite lattices were shown to achieve much higher quality factors than unipartite lattices, however, they demonstrated a less dramatic improvement in the FOM due to the sub-radiant nature of the lattices [39]. The material properties were also found to be important with Ag bipartite lattices producing a much higher FOM than Au lattices, suggesting that bipartite lattices are more dependent on LSPR scattering efficiency than unipartite lattices.

Finally, it was shown that while finite bipartite lattices show promise under ideal conditions, the introduction of structural disorder has a much more significant effect than on the unipartite lattices. A reduction in FOM to 15% of the ideal value was found for some bipartite lattices while unipartite lattices were minimally affected. This highlights the importance of considering practical fabrication errors when designing new lattices exhibiting more complex lattice resonances.

These results show that improved fabrication techniques may be required for the experimental realisation of high Q bipartite lattice resonances. Methods such as annealing or careful design of the individual elements may reduce the impact of disorder. By overcoming these potential fabrication issues we expect that bipartite lattices could be applied to applications where high quality factor optical resonances are critical, such as lasers [38] or sensors [16–19].

**Acknowledgments.** A.W. acknowledges support from the University of Canterbury College of Engineering PhD Scholarship.

**Disclosures.** The authors declare no conflicts of interest.

**Data availability.** Data underlying the results presented in this paper are not publicly available at this time but may be obtained from the authors upon reasonable request.

**Supplemental document.** See [Supplement 1](#) for supporting content.

## References

1. S. I. Azzam, A. V. Kildishev, R.-M. Ma, C.-Z. Ning, R. Oulton, V. M. Shalaev, M. I. Stockman, J.-L. Xu, and X. Zhang, “Ten years of spasers and plasmonic nanolasers,” *Light Sci Appl* **9**(1), 1–21 (2020).
2. W. Zhou, M. Dridi, J. Y. Suh, C. H. Kim, D. T. Co, M. R. Wasielewski, G. C. Schatz, and T. W. Odom, “Lasing action in strongly coupled plasmonic nanocavity arrays,” *Nat. Nanotechnol.* **8**(7), 506 (2013).
3. A. H. Schokker and A. F. Koenderink, “Lasing at the band edges of plasmonic lattices,” *Phys. Rev. B* **90**(15), 155452 (2014).
4. A. Yang, T. B. Hoang, M. Dridi, C. Deeb, M. H. Mikkelsen, G. C. Schatz, and T. W. Odom, “Real-time tunable lasing from plasmonic nanocavity arrays,” *Nat. Commun.* **6**, 1–7 (2015).
5. N. Yu and F. Capasso, “Flat optics with designer metasurfaces,” *Nature Mater* **13**(2), 139–150 (2014).
6. S. Lal, S. Link, and N. J. Halas, “Nano-optics from sensing to waveguiding,” *Nature Photon* **1**(11), 641–648 (2007).
7. A. D. Humphrey and W. L. Barnes, “Plasmonic surface lattice resonances on arrays of different lattice symmetry,” *Phys. Rev. B* **90**(7), 075404 (2014).
8. S. A. Maier, *Plasmonics: fundamentals and applications* (Springer Science & Business Media, 2007).
9. V. G. Kravets, A. V. Kabashin, W. L. Barnes, and A. N. Grigorenko, “Plasmonic surface lattice resonances: a review of properties and applications,” *Chem. Rev.* **118**(12), 5912–5951 (2018).
10. K. T. Carron, W. Fluhr, M. Meier, A. Wokaun, and H. Lehmann, “Resonances of two-dimensional particle gratings in surface-enhanced raman scattering,” *J. Opt. Soc. Am. B* **3**(3), 430–440 (1986).
11. S. Zou, N. Janel, and G. C. Schatz, “Silver nanoparticle array structures that produce remarkably narrow plasmon lineshapes,” *J. Chem. Phys.* **120**(23), 10871–10875 (2004).
12. V. G. Kravets, F. Schedin, and A. N. Grigorenko, “Extremely narrow plasmon resonances based on diffraction coupling of localized plasmons in arrays of metallic nanoparticles,” *Phys. Rev. Lett.* **101**(8), 087403 (2008).
13. R. Gómez-Medina, M. Laroche, and J. J. Sáenz, “Extraordinary optical reflection from sub-wavelength cylinder arrays,” *Opt. Express* **14**(9), 3730–3737 (2006).
14. D. R. Abujetas, J. A. Sanchez-Gil, and J. J. Sáenz, “Generalized brewster effect in high-refractive-index nanorod-based metasurfaces,” *Opt. Express* **26**(24), 31523–31541 (2018).
15. V. I. Zakmirnyi, S. V. Karpov, H. Ågren, and I. L. Rasskazov, “Collective lattice resonances in disordered and quasi-random all-dielectric metasurfaces,” *J. Opt. Soc. Am. B* **36**(7), E21–E29 (2019).

16. B. D. Thackray, V. G. Kravets, F. Schedin, G. Auton, P. A. Thomas, and A. N. Grigorenko, "Narrow collective plasmon resonances in nanostructure arrays observed at normal light incidence for simplified sensing in asymmetric air and water environments," *ACS Photonics* **1**(11), 1116–1126 (2014).
17. R. R. Gutha, S. M. Sadeghi, C. Sharp, and W. J. Wing, "Biological sensing using hybridization phase of plasmonic resonances with photonic lattice modes in arrays of gold nanoantennas," *Nanotechnology* **28**(35), 355504 (2017).
18. A. Danilov, G. Tselikov, F. Wu, V. G. Kravets, I. Ozerov, F. Bedu, A. N. Grigorenko, and A. V. Kabashin, "Ultra-narrow surface lattice resonances in plasmonic metamaterial arrays for biosensing applications," *Biosens. Bioelectron.* **104**, 102–112 (2018).
19. V. Gupta, P. T. Robst, F. R. Göbner, A. M. Steiner, J. Schubert, Y. Brasse, T. A. König, and A. Fery, "Mechanotunable surface lattice resonances in the visible optical range by soft lithography templates and directed self-assembly," *ACS Appl. Mater. Interfaces* **11**(31), 28189–28196 (2019).
20. J. Hu, D. Wang, D. Bhowmik, T. Liu, S. Deng, M. P. Knudson, X. Ao, and T. W. Odom, "Lattice-resonance metalenses for fully reconfigurable imaging," *ACS Nano* **13**(4), 4613–4620 (2019).
21. C. U. Hail, G. Schoering, M. Damak, D. Poulikakos, and H. Eghlidi, "A plasmonic painter's method of color mixing for a continuous red–green–blue palette," *ACS Nano* **14**(2), 1783–1791 (2020).
22. S. Zou and G. C. Schatz, "Narrow plasmonic/photonic extinction and scattering line shapes for one and two dimensional silver nanoparticle arrays," *J. Chem. Phys.* **121**(24), 12606–12612 (2004).
23. Q. Le-Van, E. Zoethout, E.-J. Geluk, M. Ramezani, M. Berghuis, and J. Gómez Rivas, "Enhanced quality factors of surface lattice resonances in plasmonic arrays of nanoparticles," *Adv. Opt. Mater.* **7**, 1801451 (2019).
24. A. H. Schokker and A. F. Koenderink, "Statistics of randomized plasmonic lattice lasers," *ACS Photonics* **2**(9), 1289–1297 (2015).
25. J. B. Khurgin and G. Sun, "Impact of disorder on surface plasmons in two-dimensional arrays of metal nanoparticles," *Appl. Phys. Lett.* **94**(22), 221111 (2009).
26. Y. Nishijima, L. Rosa, and S. Juodkazis, "Surface plasmon resonances in periodic and random patterns of gold nano-disks for broadband light harvesting," *Opt. Express* **20**(10), 11466–11477 (2012).
27. B. Auguie and W. L. Barnes, "Diffractive coupling in gold nanoparticle arrays and the effect of disorder," *Opt. Lett.* **34**(4), 401–403 (2009).
28. S. De Zuani, M. Rommel, R. Vogelgesang, J. Weis, B. Gompf, M. Dressel, and A. Berrier, "Large-area two-dimensional plasmonic meta-glasses and meta-crystals: a comparative study," *Plasmonics* **12**(5), 1381–1390 (2017).
29. B. Vasić and R. Gajić, "Plasmonic photonic bandgaps robust to disorder in two-dimensional plasmonic crystals," *J. Opt. Soc. Am. B* **29**(10), 2964–2970 (2012).
30. A. Tittl, M. G. Harats, R. Walter, X. Yin, M. Schaäferling, N. Liu, R. Rapaport, and H. Giessen, "Quantitative angle-resolved small-spot reflectance measurements on plasmonic perfect absorbers: impedance matching and disorder effects," *ACS Nano* **8**(10), 10885–10892 (2014).
31. M. Albooyeh, S. Kruk, C. Menzel, C. Helgert, M. Kroll, A. Krysinski, M. Decker, D. N. Neshev, T. Pertsch, C. Etrich, C. Rockstuhl, S. A. Tretyakov, C. R. Simovski, and Y. S. Kivshar, "Resonant metasurfaces at oblique incidence: interplay of order and disorder," *Sci. Rep.* **4**(1), 1–7 (2014).
32. A. Alu and N. Engheta, "Effect of small random disorders and imperfections on the performance of arrays of plasmonic nanoparticles," *New J. Phys.* **12**(1), 013015 (2010).
33. L. Zundel and A. Manjavacas, "Finite-size effects on periodic arrays of nanostructures," *J. Phys. Photonics* **1**(1), 015004 (2018).
34. F. Zhang, F. Tang, X. Xu, P.-M. Adam, J. Martin, and J. Plain, "Influence of order-to-disorder transitions on the optical properties of the aluminum plasmonic metasurface," *Nanoscale* **12**(45), 23173–23182 (2020).
35. B. D. Lucas, J.-S. Kim, C. Chin, and L. J. Guo, "Nanoimprint lithography based approach for the fabrication of large-area, uniformly-oriented plasmonic arrays," *Adv. Mater.* **20**, 1129–1134 (2008).
36. M. H. Lee, M. D. Huntington, W. Zhou, J.-C. Yang, and T. W. Odom, "Programmable soft lithography: solvent-assisted nanoscale embossing," *Nano Lett.* **11**(2), 311–315 (2011).
37. I. Staude, A. E. Miroschnichenko, M. Decker, N. T. Fofang, S. Liu, E. Gonzales, J. Dominguez, T. S. Luk, D. N. Neshev, I. Brener, and Y. Kivshar, "Tailoring directional scattering through magnetic and electric resonances in subwavelength silicon nanodisks," *ACS Nano* **7**(9), 7824–7832 (2013).
38. T. Hakala, H. Rekola, A. Väkeväinen, J.-P. Martikainen, M. Nečada, A. Moilanen, and P. Törmä, "Lasing in dark and bright modes of a finite-sized plasmonic lattice," *Nat. Commun.* **8**(1), 1–7 (2017).
39. A. Cuartero-González, S. Sanders, L. Zundel, A. I. Fernández-Domínguez, and A. Manjavacas, "Super- and subradiant lattice resonances in bipartite nanoparticle arrays," *ACS Nano* **14**(9), 11876–11887 (2020).
40. J. Sung, E. M. Hicks, R. P. Van Duyne, and K. G. Spears, "Nanoparticle spectroscopy: Plasmon coupling in finite-sized two-dimensional arrays of cylindrical silver nanoparticles," *J. Phys. Chem. C* **112**(11), 4091–4096 (2008).
41. D. Wang, A. Yang, A. J. Hryn, G. C. Schatz, and T. W. Odom, "Superlattice plasmons in hierarchical Au nanoparticle arrays," *ACS Photonics* **2**(12), 1789–1794 (2015).
42. A. D. Humphrey, N. Meinzer, T. A. Starkey, and W. L. Barnes, "Surface lattice resonances in plasmonic arrays of asymmetric disc dimers," *ACS Photonics* **3**(4), 634–639 (2016).
43. D. R. Abujetas, N. Van Hoof, S. ter Huurne, J. G. Rivas, and J. A. Sánchez-Gil, "Spectral and temporal evidence of robust photonic bound states in the continuum on terahertz metasurfaces," *Optica* **6**(8), 996–1001 (2019).
44. P. B. Johnson and R.-W. Christy, "Optical constants of the noble metals," *Phys. Rev. B* **6**(12), 4370 (1972).

45. G. Vecchi, V. Giannini, and J. G. Rivas, "Surface modes in plasmonic crystals induced by diffractive coupling of nanoantennas," *Phys. Rev. B* **80**(20), 201401 (2009).
46. S. Rodriguez, M. Schaafsma, A. Berrier, and J. G. Rivas, "Collective resonances in plasmonic crystals: Size matters," *Physica B: Condensed Matter* **407**(20), 4081–4085 (2012).
47. S. R. K. Rodriguez, A. Abass, B. Maes, O. T. Janssen, G. Vecchi, and J. G. Rivas, "Coupling bright and dark plasmonic lattice resonances," *Phys. Rev. X* **1**(2), 021019 (2011).
48. A. Egel, S. W. Kettlitz, and U. Lemmer, "Efficient evaluation of sommerfeld integrals for the optical simulation of many scattering particles in planarly layered media," *J. Opt. Soc. Am. A* **33**(4), 698–706 (2016).
49. K. M. Czajkowski, M. Bancerek, and T. J. Antosiewicz, "Multipole analysis of substrate-supported dielectric nanoresonator metasurfaces via the t-matrix method," *Phys. Rev. B* **102**(8), 085431 (2020).
50. T. J. Antosiewicz and T. Tarkowski, "Localized surface plasmon decay pathways in disordered two-dimensional nanoparticle arrays," *ACS Photonics* **2**(12), 1732–1738 (2015).
51. A. Manjavacas, L. Zundel, and S. Sanders, "Analysis of the limits of the near-field produced by nanoparticle arrays," *ACS Nano* **13**(9), 10682–10693 (2019).
52. W. A. Murray and W. L. Barnes, "Plasmonic materials," *Adv. Mater.* **19**, 3771–3782 (2007).
53. H. Gao, J. Henzie, M. H. Lee, and T. W. Odom, "Screening plasmonic materials using pyramidal gratings," *Proceedings of the National Academy of Sciences* **105**(51), 20146–20151 (2008).
54. A. Warren, M. M. Alkaisi, and C. P. Moore, "Subradiant resonances in au and ag bipartite lattices in the visible spectrum," *Journal of Vacuum Science & Technology B* **39**(6), 063601 (2021).
55. S. Deng, R. Li, J.-E. Park, J. Guan, P. Choo, J. Hu, P. J. Smeets, and T. W. Odom, "Ultrathin plasmon resonances from annealed nanoparticle lattices," *Proc Natl Acad Sci USA* **117**(38), 23380–23384 (2020).